Electronic Supplementary Information (ESI)

Surfactant-mediated mesoscopic confinement and selective interfacial shielding for highly stable zinc anode

Zhenhai Shi, Suli Chen, Min Zan, Leiqian Zhang, Jiaming Gong, Yazhou Zhou, Klaus Müllen, Feili Lai*, Tianxi Liu**

Z. H. Shi, Dr. S. L. Chen, M. Zan, L. Q. Zhang, Prof. T. X. Liu

The Key Laboratory of Synthetic and Biological Colloids, Ministry of Education, School of Chemical and Material Engineering, Jiangnan University, Wuxi, 214122, P. R. China. E-mail: chensl@jiangnan.edu.cn; txliu@jiangnan.edu.cn

J. M. Gong, Dr. F. L. Lai

State Key Laboratory of Metal Matrix Composites, School of Materials Science and Engineering, Shanghai Jiao Tong University Shanghai, 200240, P. R. China. E-mail: feililai@sjtu.edu.cn

Prof. Y. Z. Zhou

Nanotechnology Centre, Centre for Energy and Environmental Technologies, VŠB–Technical University of Ostrava17. listopadu 2172/15, Ostrava-Poruba 70800, Czech Republic

Prof. K. Müllen

Department of Molecular Spectroscopy, Max Planck Institute for Polymer Research Ackermannweg 10, Mainz 55128, Germany

Experimental Section

Materials

Zinc sulfate ($ZnSO_4$) (Aladdin Chemical Reagent Co. Ltd), sophorolipid (SL) (Wuhan Lullaby Pharmaceutical & Chemical Co., Ltd.), iodine (I_2, Macklin), carbon black, activated carbon (Guangdong Canrd New Energy Technology Co. Ltd), sodium carboxymethyl cellulose (Macklin), zinc foil, Cu foil and aluminum-plastic film (Hengyu

Metal Material Co. Ltd) in this experiment were used directly without pretreatment.

Fabrication of electrolytes

To prepare the 1 M $ZnSO_4$ aqueous electrolyte (BE), $ZnSO_4 \cdot 7H_2O$ salt was dissolved in deionized water at an appropriate molar ratio. Aqueous SL solutions with different concentrations were used to prepare the modified electrolytes, which were then sonicated to form stable mesoscopic structures in the electrolytes. The critical micelle concentration (CMC) of SL was 40 mg L^{-1}. To screen for the appropriate concentration of additives, electrolytes were prepared at concentrations of 20, 40, 80, 120, and 160 mg L^{-1}, respectively. The electrolyte at the optimal addition concentration was named BE+SL.

Fabrication of iodine cathodes

Iodine and activated carbon composites (I_2@AC) were prepared through a soaking method. Under the sonication condition, 200 mg of I_2 particles were dissolved into 1 L of deionized water. Then, 200 mg of AC was added to the above solution, sonicated and left for 6 h. Finally, the precipitate was washed with deionized water and dried at 50 °C overnight. The cathodes were made up of I_2@AC, conductive carbon black and CMC at a mass ratio of 7:2:1, using H_2O as solvent. The resulting slurry was coated on carbon cloth of 12 mm diameter, and then dried in a vacuum oven at 60 °C for 12 h. The iodine loadings on each electrode were determined based on the total mass of the electrode and the ratio of I_2@AC composite, carbon black and CMC. By controlling the volume of the slurry applied, the mass loading of the I_2 cathode is 1 mg cm^{-2} for coin cells and 5 mg cm^{-2} for pouch cells.

Material characterization

Scanning electron microscopy (SEM) and energy-dispersive X-ray spectroscopy (EDS) were characterized with a HITACHI S-4800 at 5 kV. Transmission electron microscopy (TEM) was characterized with a JEM-2100plus at 200 KV. X-ray diffraction (XRD) patterns of the samples were measured on a D8 Advance instrument (AXS-Bruker) with Cu Kα radiation. Nicolet 6700 was used to obtain the Fourier-transform infrared

spectroscopy data. The surface roughness of the Zn anode after cycling was characterized through an atomic force microscope (AFM, Bruker Dimension ICON). Thermogravimetric analysis (TGA) of I_2@AC was carried out on a NETZSCH TG209F1 Libra device. Raman spectroscopy was used to demonstrate the restructuring of the Zn^{2+} solvation shell. The distribution and composition of SL adsorption layer were characterized by XPS depth profiling (Axis supra) and ToF-SIMS mapping. Small-angle X-ray scattering (SAXS) and dynamic light scattering (DLS) were used to get the micelle size and structure.

CMC determination method

The method and principle are as follows: The surface tension of an aqueous surfactant solution decreased sharply as the concentration increased until the CMC was reached. Above the CMC, the surface tension remained relatively constant as micellization saturated the interface and bulk solution. The surface tension (γ) of SL solutions across a wide concentration range (from 5 to 90 mg L^{-1}) was measured at 25 °C. Each measurement was performed in triplicate to ensure accuracy. The CMC was identified as the distinct breakpoint in the plot of surface tension (γ) versus the logarithm of SL concentration. This breakpoint signified the concentration where micelle formation began and the surface tension plateaued. We have further confirmed the stability of the electrolyte system within the practical operating temperature range of 25 to 40°C.

Electrochemical measurements

Electrochemical tests were performed using CR2032 button cells assembled in air. The separator and electrolyte used in the symmetrical cell were glass fiber filter paper and 1 M $ZnSO_4$ aqueous solution (200 μL), respectively. Long-term cycling performance and rate capability of coin-type cells were tested by multichannel battery testing system. The voltage range for full cells was 0.6-1.6 V. The cyclic voltammetry (CV), electrochemical impedance spectroscopy (EIS), and chronoamperometry measurements (CA) were conducted by electrochemical workstation (CHI660E). Electrochemical workstation was carried out to conduct EIS within the frequency

range of 10^5-10^{-2} Hz, to perform chronoamperometry of Zn symmetric cells at an overpotential of -150 mV. EIS measurements at different temperatures were executed by using a CHI660E in a frequency range of 0.1-10^6 Hz. The various performance of coin and pouch cells was collected using LAND instruments.

Computational method

Density functional theory (DFT) calculations were performed using Gaussian 16 package,[1] B3LYP density functional and 6-311+g(d) basis set were used for all calculations, and the DFT-D3 method was used to describe dispersion correction in all calculations. Visualization of the structures was made by using VMD software. The electrostatic potential (ESP) was analyzed by Multiwfn software.[2,3] The binding energy was defined by equation 1:[4]

$$E_{\text{desolvation energy}} = E_{\text{Zn+TM}} - E_{\text{Zn}} - E_{\text{TM}} \qquad (1)$$

where $E_{\text{Zn+TM}}$ is the total energy of the structural Zn+TM, E_{Zn} is the total energy of the structural Zn, E_{TM} is the total energy of the structural TM.

Molecular dynamics (MD) simulation

MD simulation was performed through Gromacs2018.8 software[5] to study the solvated structure. The molecular geometries were optimized by Gaussian 16 package at the B3LYP/6-311+g(d) level of theory. The force field parameters of SL, Zn^{2+}, SO_4^{2-}, and H_2O were obtained with OPLS-AA force field. Atomic charges of all ions were multiplied by scale factor 0.8 to correct the polarization effect of ions. The simulation boxes were generated by packmol software.[6] These simulation boxes were constructed as follows: 1) BE system consisted of 8000 H_2O, and 150 $ZnSO_4$ molecules; 2) BE+SL system consisted of 8000 H_2O, 150 $ZnSO_4$, and 25 SL molecules. All simulation systems were first energetically minimized using the steepest descent algorithm. Atomistic simulations were further performed in a canonical ensemble (NVT) for 20 ns, and simulation trajectories were recorded at an interval of 1 ps for further structural and dynamical analysis. The VMD software[7] was used to visualize the systems and obtain the ion association state, RDF function, and distribution of

number.

COMSOL simulations

Finite element simulations were carried out using COMSOL Multiphysics 6.2, where the electric and concentration fields were modelled using a “cubic current distribution” physical field. The ion concentration followed the first law of Fick's diffusion, while the electromigration followed the Nernst-Planck relation. Both models took into account a simplified structure of the study space, with two electrodes of 10 μm length and 8 μm distance between them, and a number of nucleation sites uniformly distributed on the surface of the negative electrode, and the main body of the simulation solution was the electrode-electrolyte interface. The boundary conditions were based on the zero-potential boundary at the positive electrode, and the potential at the negative electrode was set as the polarization voltage of the cell. The initial Zn^{2+} concentration was set to 1 M. The effective diffusion coefficients of Zn^{2+} in the BE and BE+SL electrolytes were set to 3×10^{-16} and 8×10^{-16} $m^2\ s^{-1}$, respectively. The exchange current density through the cell was set to 8 mA cm^{-2}. The system temperature was set to 298 K. The electrode-electrolyte interface was set to 2.5 mA cm^{-2}.

Supplementary Figures and Tables: Fig. S1-S40, Table S1-S6

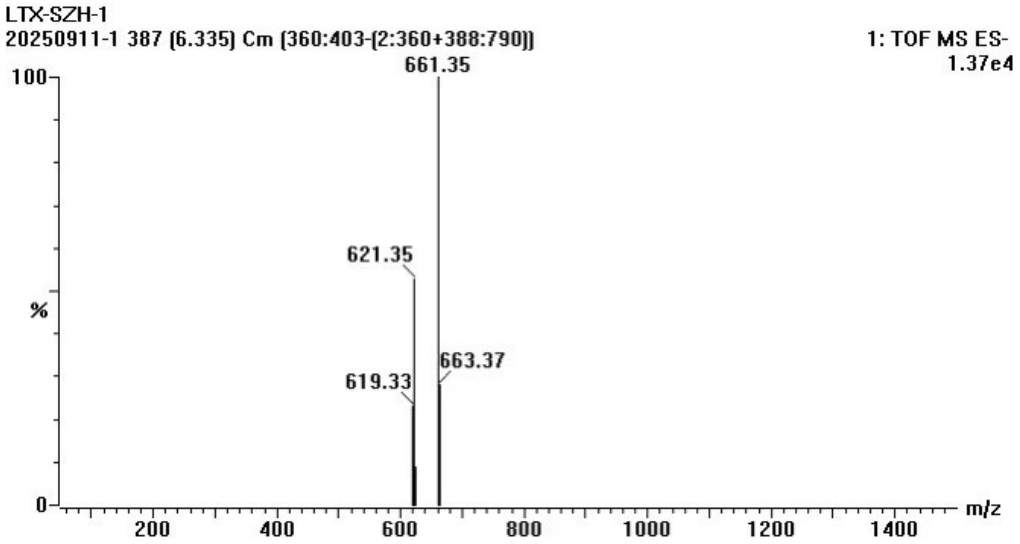

Fig. S1 Mass spectrometry of SL. ESI-TOF($C_{32}H_{56}O_{14}$): 663.37($M\text{-}H^+$), 621.35($M\text{-}2H^+\text{-}Na^+\text{-}OH$), results from multiple batches are consistent.

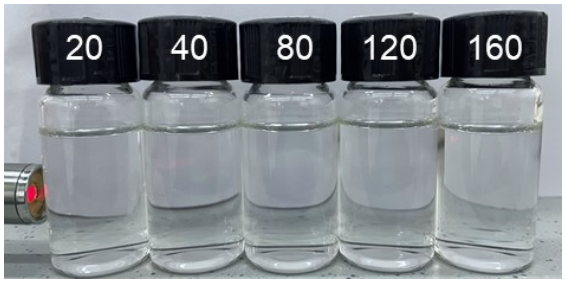

Fig. S2 Optical images of the Tyndall effect for different contents of SL in 2 M $ZnSO_4$ electrolytes.

Note: The stability of surfactant self-assembled structures was dependent on salt concentration. At low concentrations, the predominance of Zn^{2+} electrostatic shielding enhanced micelle stability. At high concentrations, the interactions of Zn^{2+} with carboxylic acid groups were exacerbated, triggering the disintegration of the micelles or the precipitation. Thus, high salt concentration led to precipitation of micellar structures and weakened Tyndall effect, while the Tyndall effect was more obvious in 1 M+40 mg L^{-1} salt solution than in 40 mg L^{-1} aqueous solution (**Fig. 2a**). Consequently, the optimal concentration of 40 mg L^{-1} SL and 1 M zinc sulfate was chosen here.

Fig. S3 Optical image of the Tyndall effect of the 1 M $ZnSO_4$ electrolyte with SL concentration of 40 mg L^{-1} after rest.

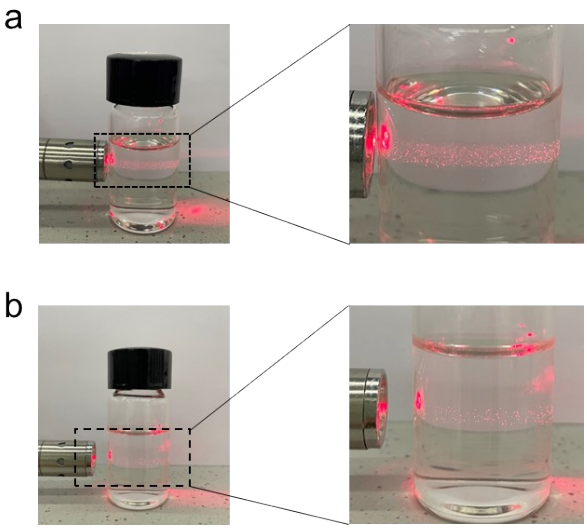

Fig. S4 Optical images of the Tyndall effect of the 1 M $ZnSO_4$ electrolytes with SL concentrations of (a) 80 and (b) 120 mg L^{-1} after one month of rest.

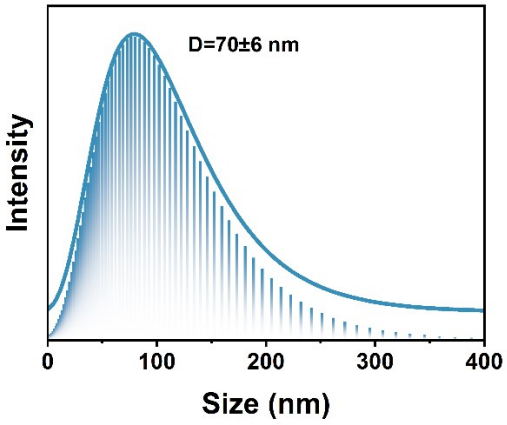

Fig. S5 The DLS size distribution histograms of SL (40 mg L^{-1}) in 1 M $ZnSO_4$ solutions.

Note: The about 70 nm value measured by DLS represents the intensity-weighted average diameter with a polydispersity index of 0.15.

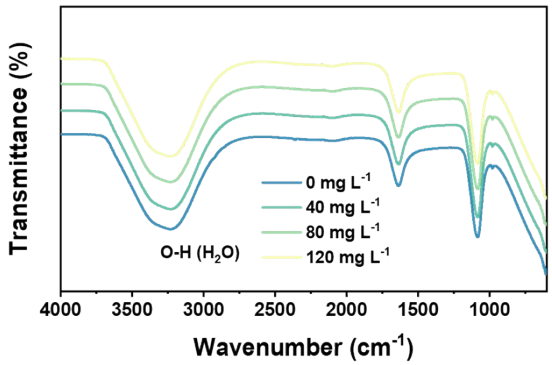

Fig. S6 FTIR spectra of BE with SL concentrations of 0, 40, 80 and 120 mg L^{-1}.

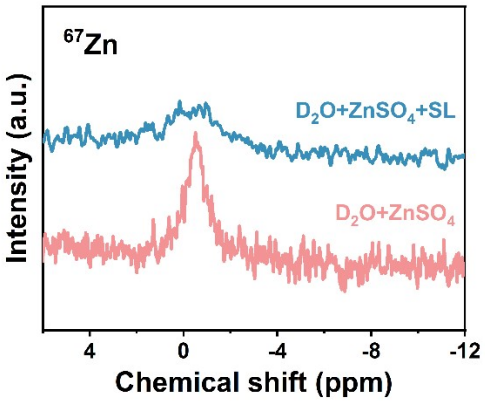

Fig. S7 ^{67}Zn NMR spectra of D_2O+$ZnSO_4$ and D_2O+$ZnSO_4$+SL solutions.

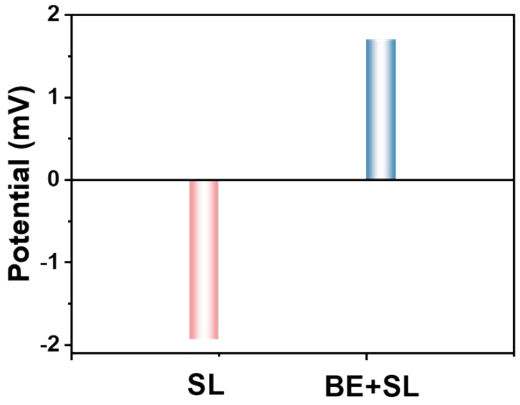

Fig. S8 Zeta potentials of SL (40 mg L^{-1}) in H_2O and 1 M $ZnSO_4$ solution.

Note: The zeta potential was measured, as evidenced by the shift from -1.97 mV in pure water to +1.7 mV in salt solution. This demonstrates that the adsorption of Zn^{2+} ions on SL micelles alters the coordination environment, which is the cornerstone of our proposed mesoscopic confinement mechanism. This charge reversal confirms that the micellar interface becomes positively charged, creating a nanoscale domain that preferentially attracts and confines Zn^{2+}, thereby rationalizing the improved transport properties.

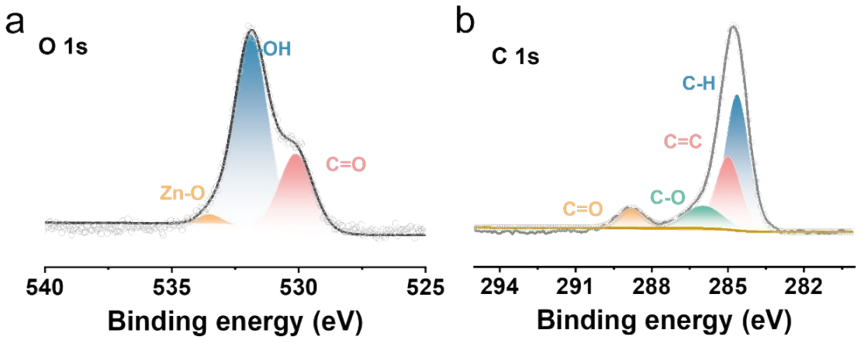

Fig. S9 (a) O 1s and (b) C 1s of XPS spectra of Zn electrodes after immersion in BE+SL.

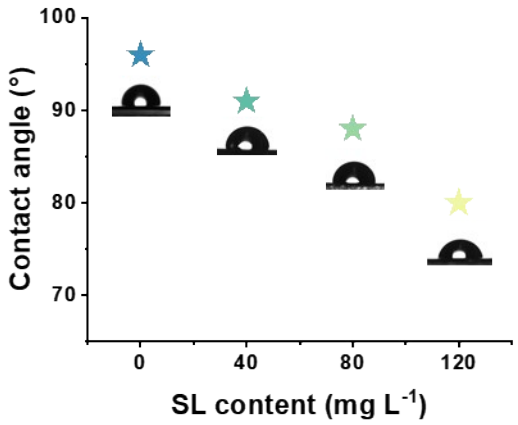

Fig. S10 Contact angle test of BE+SL solutions with different SL contents.

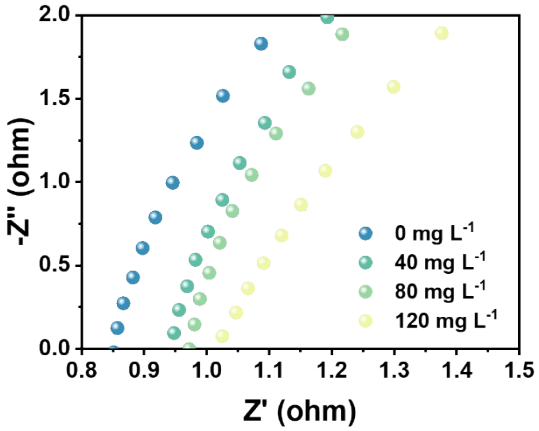

Fig. S11 EIS plots of stainless-steel symmetric cells based on different SL contents.

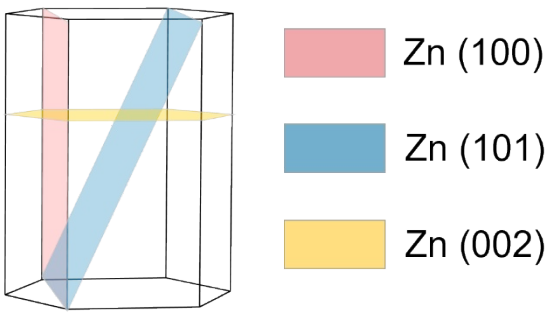

Fig. S12 Crystal structure of metallic Zn for DFT calculations.

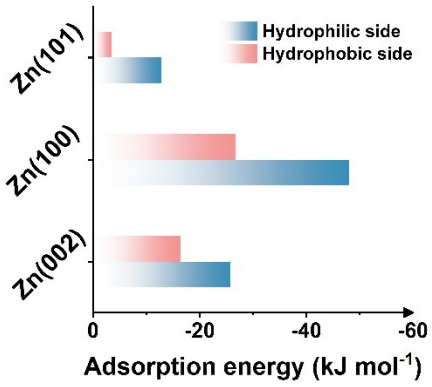

Fig. S13 Comparison of the adsorption energies of the hydrophilic and hydrophobic sides of the SL on different Zn crystal planes.

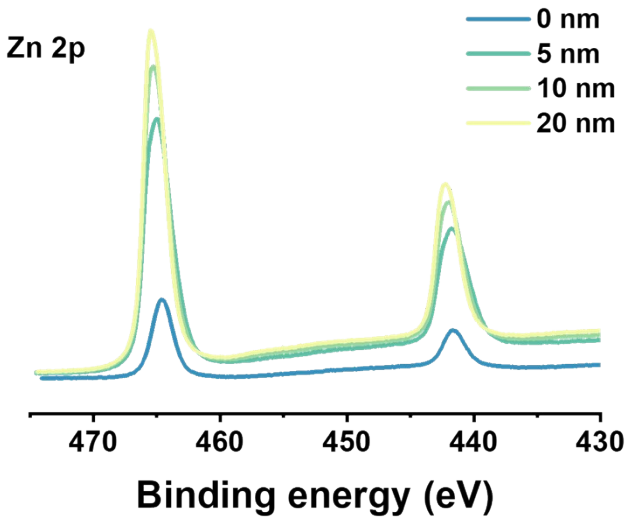

Fig. S14 The Zn 2p of XPS spectra for different sputtering depth of Zn surface after cycling in BE+SL.

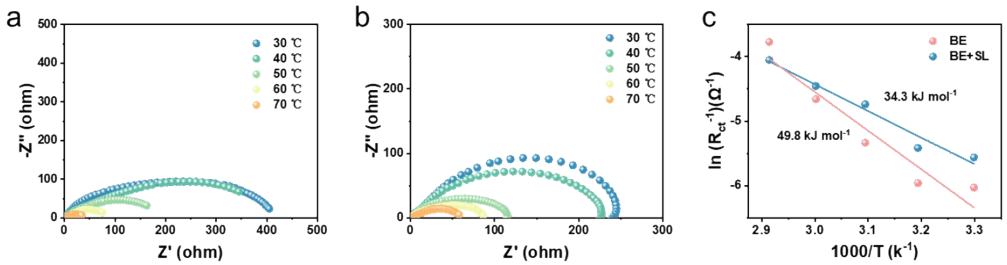

Fig. S15 EIS plots of Zn//Zn symmetric cells using (a) BE and (b) BE+SL electrolytes at different temperatures, and the corresponding (c) desolvation activation energies.

Note: The desolvation process of Zn^{2+} ions are usually considered to be a critical parameter for Zn deposition at the anode, which can be described by the activation energy (E_a) through the law of Arrhenius equation. The activation energy (E_a) for the charge transfer process on the Zn surface was measured by EIS at different temperatures (from 30 to 70 °C) in Zn//Zn symmetrical cells.

$$\frac{1}{R_{ct}} = A \exp\left(\frac{-E_a}{RT}\right) \qquad (2)$$

where R_{ct} is the interfacial resistance, A is the frequency factor, R is the gas constant, and T is the absolute temperature.

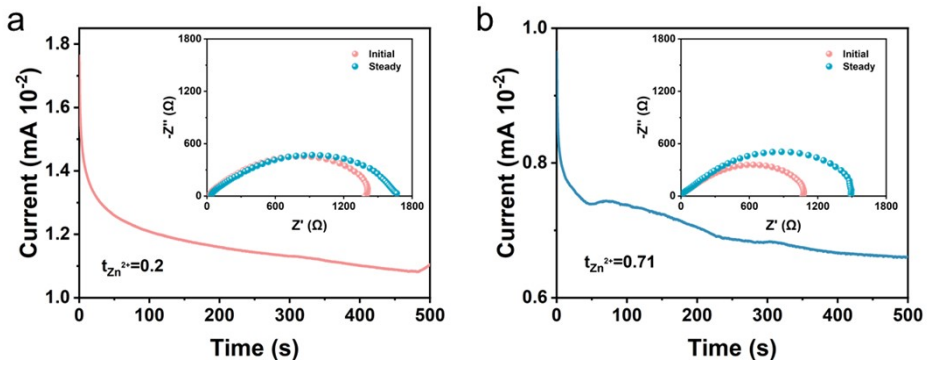

Fig. S16 Time-dependence response of polarization with an applied voltage of 25 mV at room temperature and the corresponding EIS plots of the Zn//Zn symmetric cells in (a) BE and (b) BE+SL.

Note: The Zn^{2+} transference number ($t_{Zn^{2+}}$) was determined by measuring the EIS before and after chronoamperometry. The calculation formula is as follows:

$$t_{Zn^{2+}} = \frac{I_s(\Delta V - R_o I_o)}{I_o(\Delta V - R_s I_s)} \quad (3)$$

where ΔV represents voltage polarization (25 mV in this work), I_o and R_o are the initial current and resistance, and I_s and R_s are the initial and steady-state current and resistance.

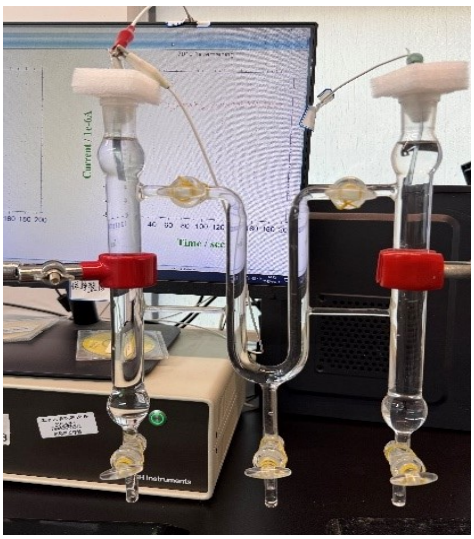

Fig. S17 Experimental setup for measuring the migration number of Zn^{2+} by the Hittorf method.

Note: The Hittorf device consists of a central chamber and two electrode chambers, interconnected by piston-operated channels to ensure complete isolation and removal of solutions from each compartment after electrolysis. The critical design feature prevents solution diffusion and mixing post-electrolysis. The overall dimensions are 30 cm in length and 21 cm in width. Each electrode chamber has a volume of 55 mL, and the intermediate chamber contains 30 mL of solvent.

The classical Hittorf method was employed to measure the migration number and exclude the influence of interface reactions (**Fig. S17**). It quantitatively assessed ion migration based on concentration changes in electrode compartments after electrolysis, which was entirely independent of interfacial impedance or side reactions. The Zn^{2+} transfer number measured by the Hittorf method was 0.67 ± 0.01, which was in excellent agreement with those obtained previously via the Bruce-Vincent method. This experiment completely eliminated disruption from interfacial effects, ultimately demonstrating that its unique micelle structure can significantly and substantially enhance the transfer number of Zn^{2+} in bulk electrolyte. The relevant data and descriptions have been incorporated into the revised manuscript.

$$t_{Zn^{2+}} = 1 + \frac{2F * \triangle n}{Q} \qquad (4)$$

where Δn is the change in the number of moles of Zn^{2+} before and after electrolysis, F is the Faraday's constant, Q is the total charge.

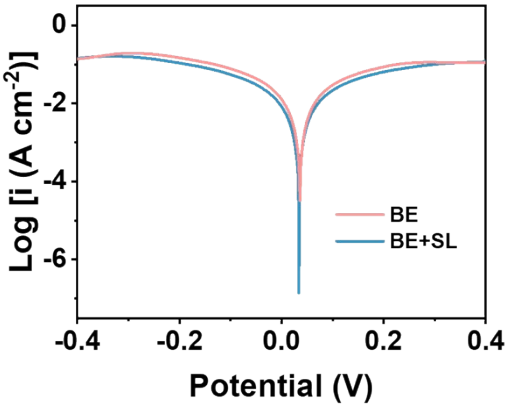

Fig. S18 Linear polarization curves of the Zn anode in BE and BE+SL electrolytes.

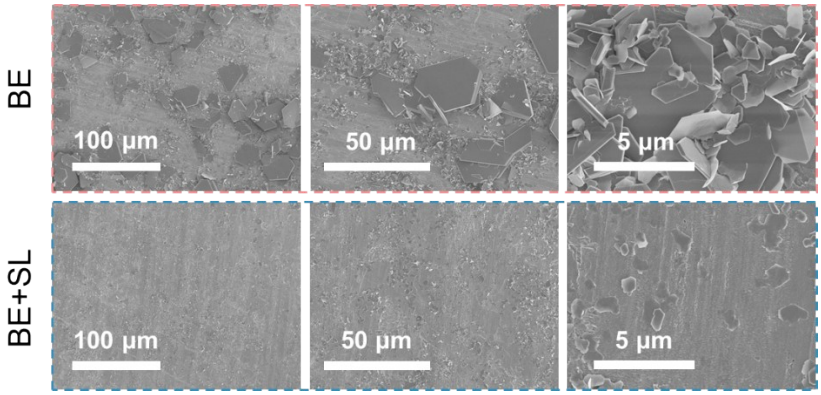

Fig. S19 SEM images of zinc anode after soaking in BE and BE+SL for 5 days.

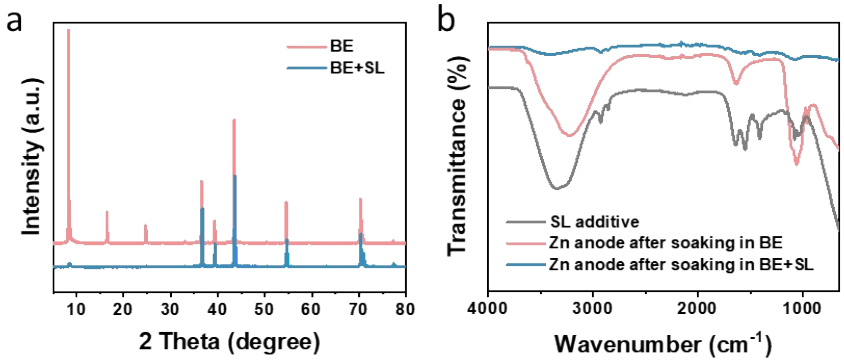

Fig. S20 (a) XRD patterns and (b) FTIR spectra of the Zn foil surfaces in different electrolytes after the immersion test.

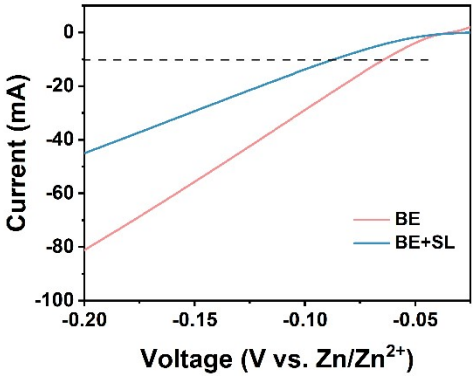

Fig. S21 LSV curves of the Zn anode in BE and BE+SL electrolytes.

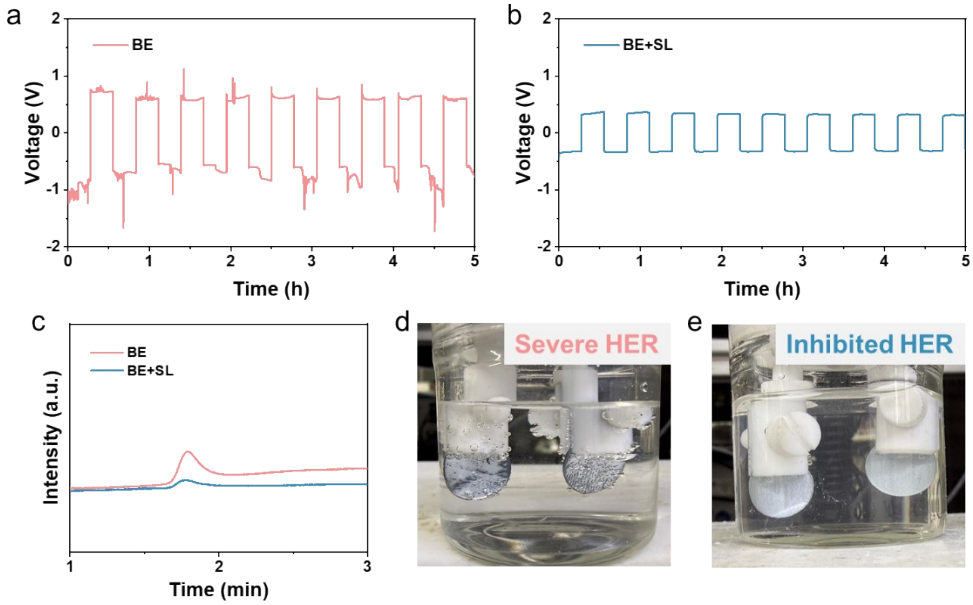

Fig. S22 (a, b) Galvanostatic charge/discharge cycling voltage profiles of the BE and BE+SL symmetric cells at 10 mA cm^{-2}. (c) In situ monitoring of hydrogen evolution flux of Zn–Zn symmetric cells with different electrolytes. Digital photo of Zn anodes in (d) BE and (e) BE+SL electrolytes after cycling.

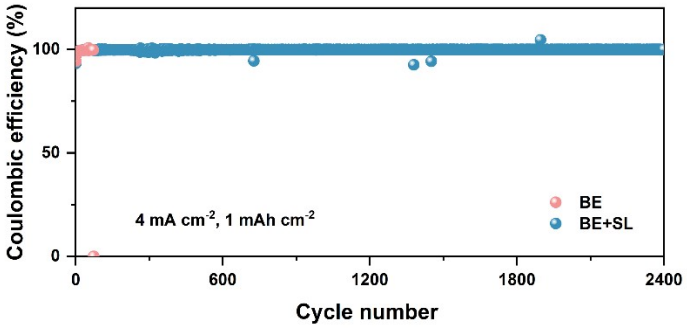

Fig. S23 The coulombic efficiency of Zn plating/stripping behavior in Zn//Cu asymmetric cells at 4 mA cm^{-2}, 1 mAh cm^{-2}.

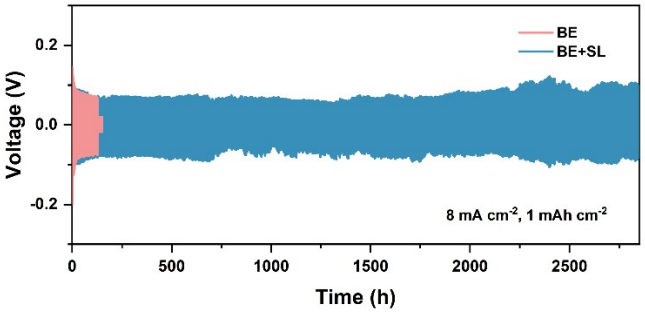

Fig. S24 Cycling performance of Zn//Zn symmetric cells with different electrolytes at a current density of 8 mA cm^{-2}, with a fixed capacity of 1 mAh cm^{-2}.

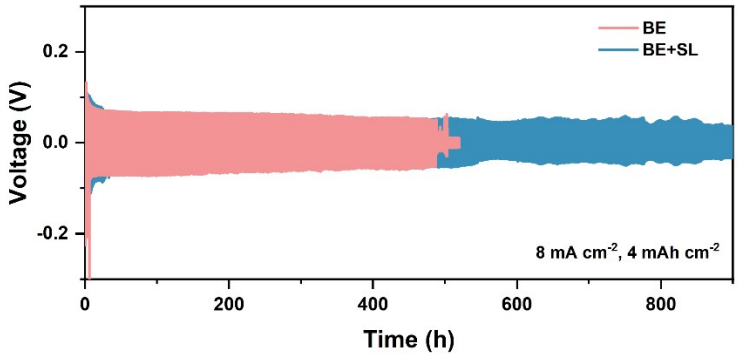

Fig. S25 Cycling performance of Zn//Zn symmetric cells with different electrolytes at a current density of 8 mA cm^{-2}, with a fixed capacity of 4 mAh cm^{-2}.

Note: When the testing current density increased to 8 mA cm^{-2}, the symmetric Zn//Zn cell in BE+SL still demonstrated a long lifespan of over 2500 h, whereas the symmetric Zn//Zn cell using BE as the electrolyte failed after 125 h, accompanied by a sudden increase in polarization voltage (**Fig. S24**). Even at 4 mAh cm^{-2}, the Zn//Zn symmetric cell in BE+SL maintained stable polarization profiles for 900 h, significantly outperforming the cell in BE (**Fig. S25**).

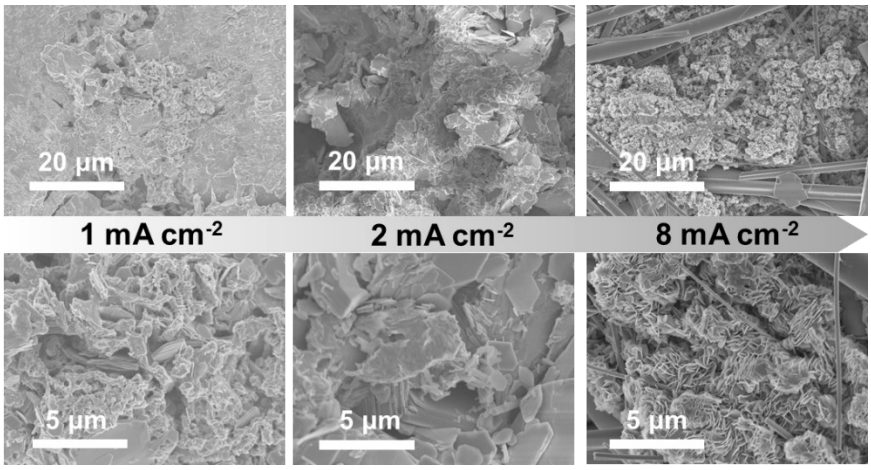

Fig. S26 SEM images of the Zn anode surface after cycling for 48 h in BE electrolyte at various current densities.

Note: To confirm the effectiveness of SL in suppressing Zn dendrite growth, Zn^{2+} ions were electrochemically plated onto Zn metal anodes at different current density using BE and BE+SL as the electrolytes, respectively. As the current density increased from 1 to 8 mA cm^{-2}, small blocky Zn began to accumulate, and the Zn surface in BE was covered with loose and irregular Zn (**Fig. S26**). In contrast, the Zn anode in BE+SL maintained a smooth and dendrite-free surface even at a high areal capacity of 8 mAh cm^{-2} (**Fig. 5a**). This result confirmed that the SL additive promoted the uniform distribution of Zn^{2+} ions, thereby inhibiting Zn dendrite growth.

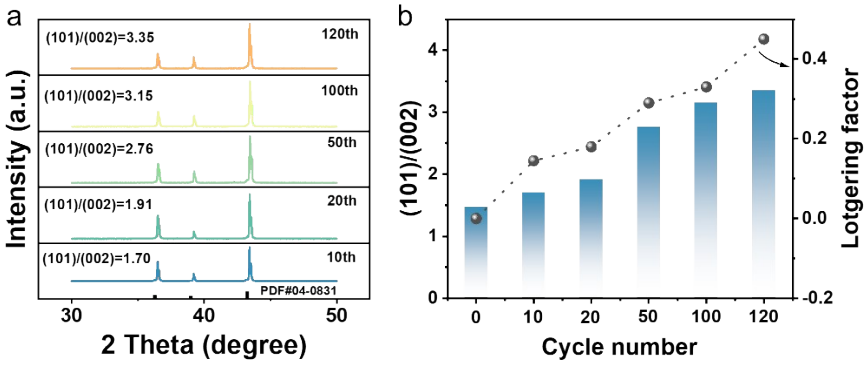

Fig. S27 (a) XRD pattern evolutions of the Zn anode surface during cycling at 1 mA cm^{-2}, 1 mAh cm^{-2}. (b) The Lotgering factor variation trends during the cycling process.

Note: The XRD analysis of the Zn anodes was performed after the indicated number of cycles to track the evolution of orientation. To quantitatively characterize the crystal orientation of Zn deposition, we adopted the Lotgering factor (LF) calculation method. The LF was defined as $f(101) = (P-P_o)/(1-P_o)$, where P was the relative intensity ratio of the (101) peak in the sample, and P_o was the relative intensity in the standard powder diffraction card (JCPDS No. 04-0831). Analysis of XRD data from anode cycling in BE+SL electrolyte indicated that the relative intensity of the (101) plane diffraction peak continuously increased with cycling, while the diffraction intensities of other planes such as (002) and (100) relatively decreased. This trend was quantified via LF calculations, as shown in **Fig. S27**. The LF value for the Zn (101) plane exhibited a significant progressive increase, clearly indicating the formation and development of (101) plane orientation preference during Zn deposition.

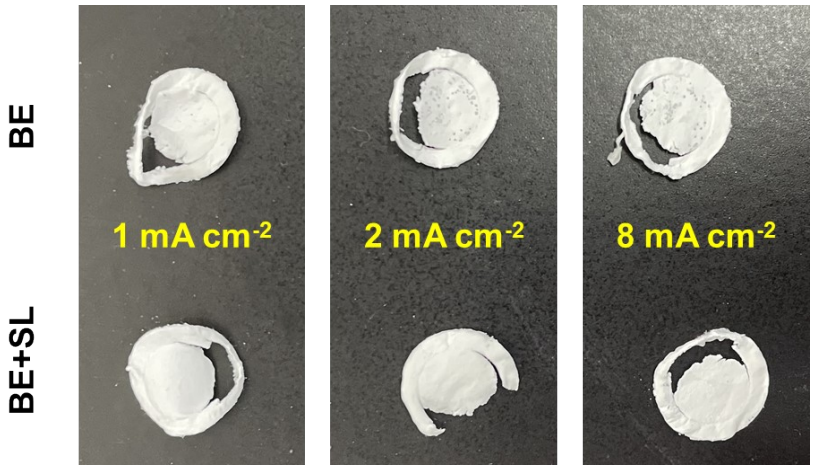

Fig. S28 Digital photographs of glass fiber separators with different electrolytes after cycling.

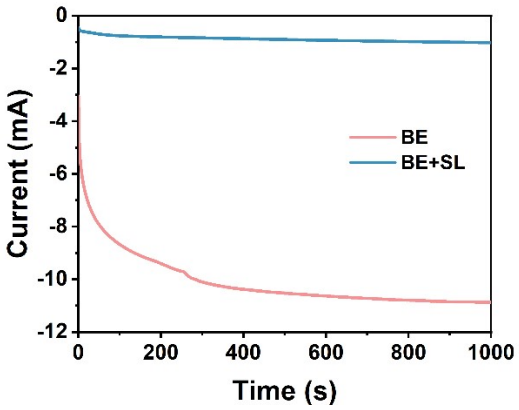

Fig. S29 Chronoamperograms (CA) in the electrolytes with or without SL at a -150 mV overpotential.

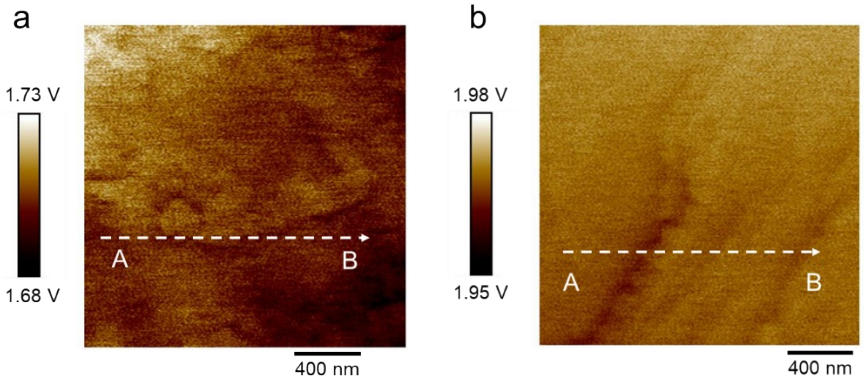

Fig. S30 Contact potential difference maps taken from the KPFM images for Zn deposition layer in (a) BE and (b) BE+SL electrolytes.

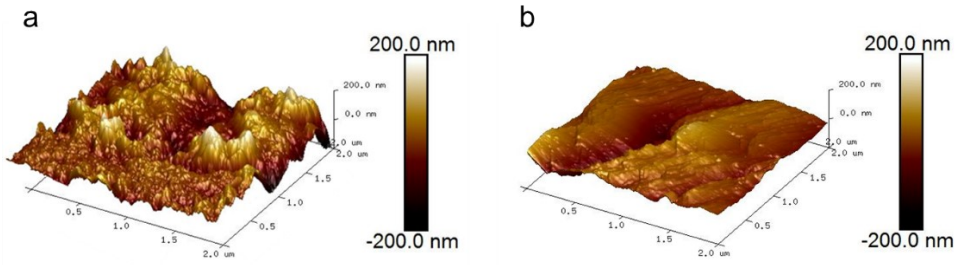

Fig. S31 The atomic force microscope 3D images of the zinc deposition layers in (a) BE and (b) BE+SL electrolytes.

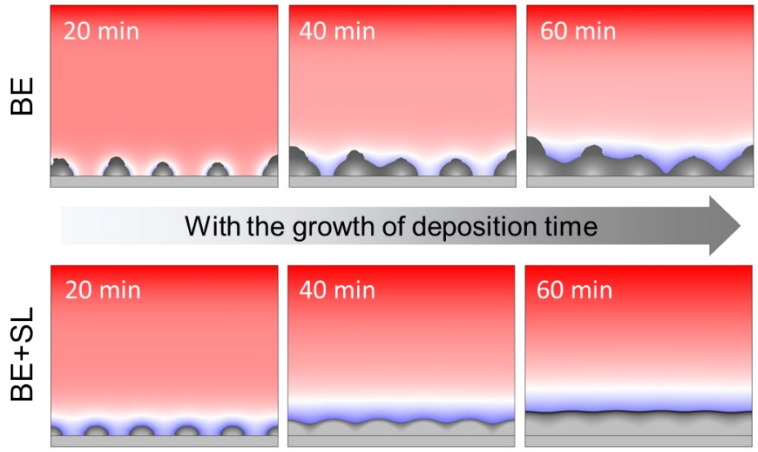

Fig. S32 COMSOL simulations of Zn^{2+} distributions for the Zn anode surface in BE and BE+SL electrolytes.

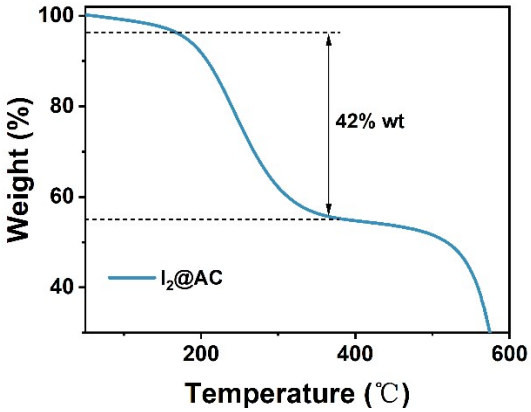

Fig. S33 Thermogravimetric curve of the I_2@AC composite.

Note: As illustrated in Fig. S33, the iodine ratio within the I_2@AC composite was estimated to be approximately 42 wt% based on thermogravimetric curve.

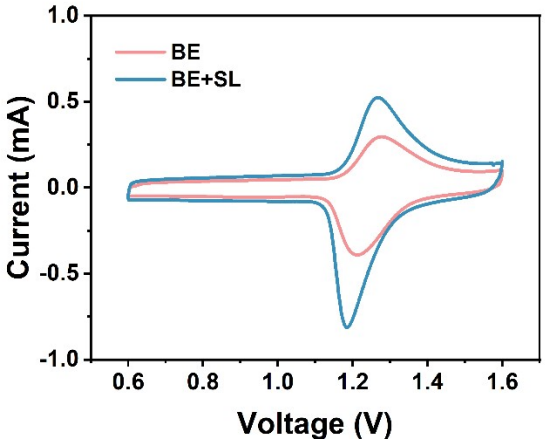

Fig. S34 CV curves of Zn//I_2 batteries at BE and BE+SL electrolytes.

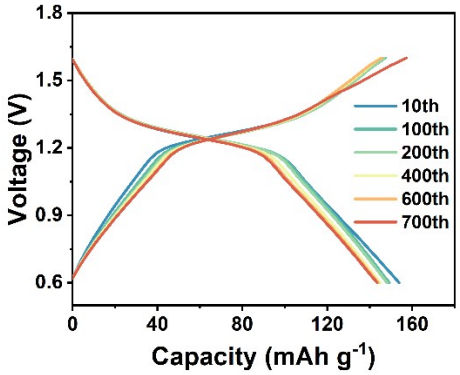

Fig. S35 Galvanostatic charge/discharge profiles of Zn//I_2 cells in BE at a current density of 0.2 A g^{-1}.

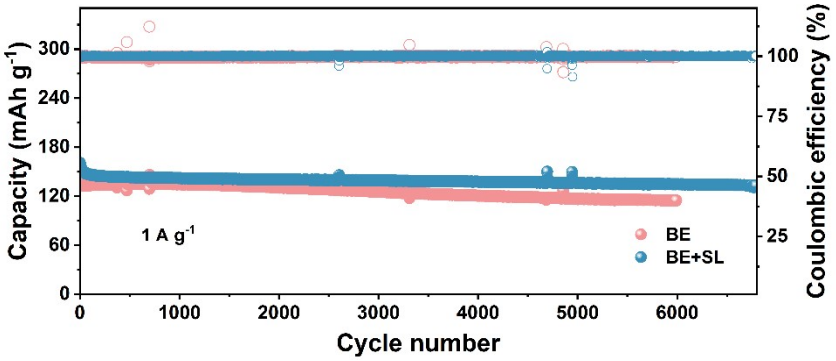

Fig. S36 Long-term stability of Zn//I_2 cells in BE and BE+SL electrolytes at a current density of 1 A g^{-1}.

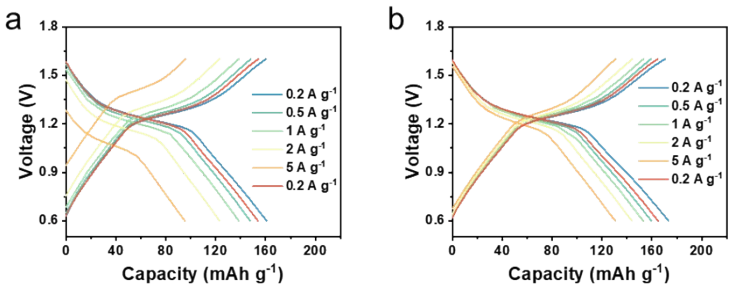

Fig. S37 Voltage profiles at different current densities of (a) BE and (b) BE+SL cells.

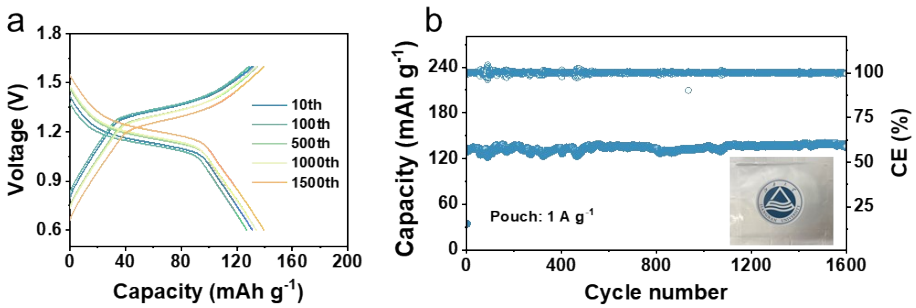

Fig. S38 (a) Charge-discharge profiles of the Zn//I_2 pouch cells in the electrolyte with SL additive at 1 A g^{-1}. (b) The cycling performance of the pouch cells with a cathode I_2 loading of approximately 5.0 mg cm^{-2}, an excess zinc anode, and a total injected electrolyte volume of 3 mL, corresponding to an E/C ratio of 108 µL mAh^{-1}.

Note: Based on the average discharge voltage and actual reversible capacity of pouch cell, the estimated mass energy density was approximately 35 Wh kg^{-1}. We explicitly noted that this estimation was based on current laboratory prototypes and excluded all non-active materials such as packaging. It aims to demonstrate application potential, while actual commercial energy density required further engineering optimization. The E/C ratio reached 108 µL mAh^{-1}, indicating that the system was in an electrolyte-enriched state. This condition was employed to validate the intrinsic stability and ultra-long cycle life of the SL additive.

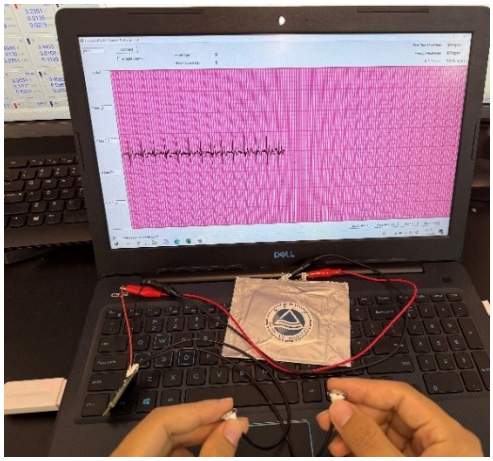

Fig. S39 Digital photograph of a pouch cell powering a heart rate monitoring device.

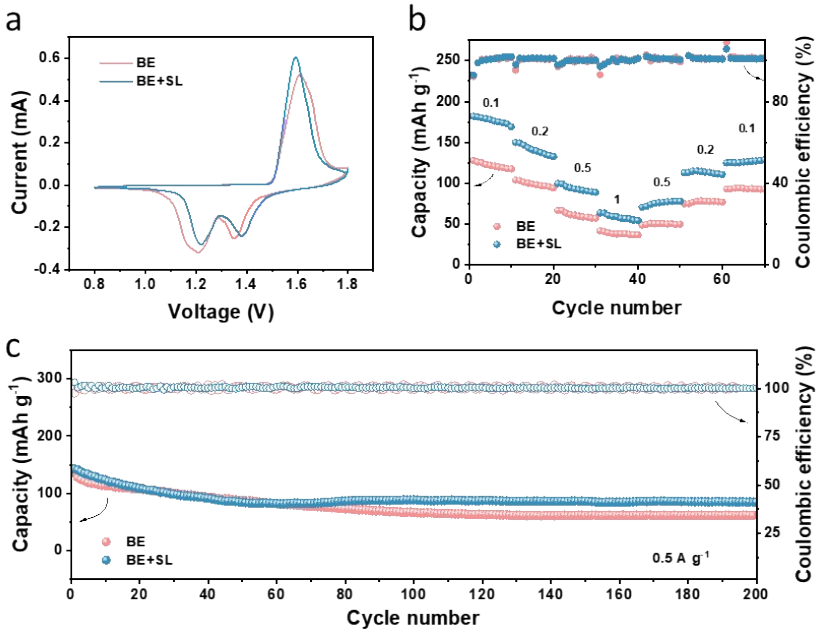

Fig. S40 Electrochemical performance of Zn//Mn full cells. (a) CV profiles of the Zn//MnO_2 cells with BE and BE+SL electrolytes at 0.1 mV s^{-1}. (b) Rate capability of Zn//MnO_2 full cells. (c) Long-term cycling performance at 0.5 A g^{-1}.

Note: Fig. S40a showed the CV curves measured at 0.1 mV s^{-1}. The Zn//MnO_2 cells showed similar CV shapes with different electrolytes, indicating the introduction of SL did not change the electrochemical mechanism of MnO_2 cathode. In addition, the area of the CV curve of BE+SL was larger than that of BE, which suggested that the SL was favorable to the Zn^{2+} diffusion process. The Zn//MnO_2 with SL cell also exhibited excellent rate capability with a much higher specific capacity than the Zn//MnO_2 cell (**Fig. S40b**). From **Fig. S40c**, the full cell with the SL still delivered excellent long-term cycling stability at 0.5 A g^{-1}, presenting no apparent capacity degradation.

Table S1. Summary of Raman spectra fitting analysis results.

SL content (mg L^{-1})	0	40	80	120
Strong hydrogen bond (%)	8.1	9.3	20.2	21.1
Medium hydrogen bond (%)	70.8	67.5	58	57.2
Weak hydrogen bond (%)	21.1	23.2	21.8	21.5
$\nu(SO_4^{2-})$ peak position (cm^{-1})	996.48	996.95	997.22	997.35

Table S2. Transport number for BE+SL electrolyte.

Parameters	BE+SL	Unit
Ion transport number	0.71	-
Polarization voltage (ΔV)	0.025	V
Initial current (I_o)	9.2×10^{-6}	A
Steady state current (I_s)	6.58×10^{-6}	A
Initial interfacial resistance (R_o)	1102	Ω
Steady interfacial resistance (R_s)	1506	Ω

Table S3. Transport number for BE electrolyte.

Parameters	BE	Unit
Ion transport number	0.20	-
Polarization voltage (ΔV)	0.025	V
Initial current (I_o)	1.6×10^{-5}	A
Steady state current (I_s)	1.1×10^{-5}	A
Initial interfacial resistance (R_o)	1405	Ω
Steady interfacial resistance (R_s)	1751	Ω

Table S4. The parameters of corrosion rate (CR) for BE and BE+SL electrolytes.

Parameters	BE	BE+SL	Unit
Mass loss (ΔW)	1.1	0.3	mg
Time (t)	120	120	h
Density (ρ)	7.14	7.14	g cm^{-3}
Area (A)	1.1304	1.1304	cm^2
Corrosion rate (CR)	**0.10**	**0.027**	**mm $year^{-1}$**

Note: We conducted a standardized immersion test according to ASTM G31-72. Zn foils were immersed in BE and BE+SL electrolytes for 120 h at 25 °C. The corrosion rate (CR) was calculated from the mass loss using the formula: CR (mm $year^{-1}$) = (8.76×10^4 × ΔW) / (A × t × ρ), where ΔW is the mass loss (mg), A is the area (cm^2), t is time (h), and ρ is the density (g cm^{-3}). The average corrosion rate for Zn in BE was 0.10 mm $year^{-1}$. The average corrosion rate in BE+SL was 0.027 mm $year^{-1}$, representing an about 73% reduction. This data is now included in **Table S4**.

Table S5. Comparison of the cycling lifespan at different current densities and capacities of this work with other reported electrolyte additives.

Additive	Additive content	Electrolyte	Current density (mAh cm^{-2})	Areal capacity (mAh cm^{-2})	Cumulative plating capacity (mAh cm^{-2})	Ref.
SL	**0.04 mg mL^{-1}**	**1 M**	**1 8 8**	**1 4 8**	**2800 4000 7200**	**This work**
LBG	0.1 wt%	1 M	2	2	2200	[8]
TA-Na	0.01 M	1 M	0.5	0.25	750	[9]
LiCl	2 M	1 M	2 5	2 5	350 800	[10]
NMP	5%	1 M	1	1	600	[11]
AN	10%	1 M	1 2	1 2	600 1200	[12]
TG	10%	1 M	1	0.5	1100	[13]
CCl	1 mg mL^{-1}	1 M	1	1	1100	[14]
PASP	8 mg mL^{-1}	1 M	0.5	0.5	1500	[15]
SF	0.5 wt%	1 M	1	1	1600	[16]
HEI	10%	1 M	5	5	750	[17]
TDFND	5 mM	1 M	1	1	1200	[18]
$La(NO_3)_3$	0.368	1 M	1	1	1200	[19]
NMS	10%	1 M	1 5	1 5	2000 6000	[20]

Table S6. Comparison of SL strategy and typical artificial SEI strategy.

Strategy	**COF/MOF**[21-23]	**Gel**[24-26]	**This work**
Complexity	High (Multi-step)	Medium	Ultra-low
Thickness	Tens to hundreds of nm	Micrometer-scale	Molecularly thin
Resistance	Variable resistance	high resistance	small resistance
Cost	High	Medium/High	Ultra-low
Sustainability	Low (organic solvents, energy consumption)	Low (poor degradability)	High (Bio-sourced)

References

1 M. J. Frisch, G. W. Trucks, H. B. Schlegel, G. E. Scuseria, M. A. Robb, J. R. Cheeseman, G. Scalmani, V. Barone, G. A. Petersson, H. Nakatsuji, X. Li, M. Caricato, A. V. Marenich, J. Bloino, B. G. Janesko, R. Gomperts, B. Mennucci, H. P. Hratchian, J. V. Ortiz, A. F. Izmaylov, J. L. Sonnenberg, Williams, F. Ding, F. Lipparini, F. Egidi, J. Goings, B. Peng, A. Petrone, T. Henderson, D. Ranasinghe, V. G. Zakrzewski, J. Gao, N. Rega, G. Zheng, W. Liang, M. Hada, M. Ehara, K. Toyota, R. Fukuda, J. Hasegawa, M. Ishida, T. Nakajima, Y. Honda, O. Kitao, H. Nakai, T. Vreven, K. Throssell, J. A. Montgomery Jr., J. E. Peralta, F. Ogliaro, M. J. Bearpark, J. J. Heyd, E. N. Brothers, K. N. Kudin, V. N. Staroverov, T. A. Keith, R. Kobayashi, J. Normand, K. Raghavachari, A. P. Rendell, J. C. Burant, S. S. Iyengar, J. Tomasi, M. Cossi, J. M. Millam, M. Klene, C. Adamo, R. Cammi, J. W. Ochterski, R. L. Martin, K. Morokuma, O. Farkas, J. B. Foresman, D. J. Fox Wallingford, CT, 2016.

2 J. Zhang, T. Lu, *PCCP* 2021, **23**, 20323.

3 T. Lu, F. W. Chen, *J. Comput. Chem.* 2012, **33**, 580.

4 D. Wang, H. Liu, F. Liu, G. Ma, J. Yang, X. Gu, M. Zhou, Z. Chen, *Nano Lett.* 2021, **21**, 4757.

5 M. J. Abraham, T. Murtola, R. Schulz, S. Páll, J. C. Smith, B. Hess, E. Lindahl, *SoftwareX* 2015, **1-2**, 19.

6 L. Martínez, R. Andrade, E. G. Birgin, J. M. Martínez, 2009, **30**, 2157.

7 W. Humphrey, A. Dalke, K. Schulten, *J. Mol. Graphics* 1996, **14**, 33.

8 K. Wang, H. Zhan, W. Su, X.-X. Liu, X. Sun, *Energy Environ. Sci.* 2025, DOI:10.1039/D4EE04100C 10.1039/D4EE04100C.

9 J. Wan, R. Wang, Z. Liu, L. Zhang, F. Liang, T. Zhou, S. Zhang, L. Zhang, Q. Lu, C. Zhang, Z. Guo, *ACS Nano* 2023, **17**, 1610.

10 X. Guo, Z. Zhang, J. Li, N. Luo, G.-L. Chai, T. S. Miller, F. Lai, P. Shearing, D. J. L. Brett, D. Han, Z. Weng, G. He, I. P. Parkin, *ACS Energy Lett.* 2021, **6**, 395.

11 T. C. Li, Y. Lim, X. L. Li, S. Luo, C. Lin, D. Fang, S. Xia, Y. Wang, H. Y. Yang, *Adv. Energy Mater.* 2022, **12**, 2103231.

12 Z. Hou, H. Tan, Y. Gao, M. Li, Z. Lu, B. Zhang, *J. Mater. Chem. A* 2020, **8**, 19367.

13 Z. Liu, R. Wang, Q. Ma, J. Wan, S. Zhang, L. Zhang, H. Li, Q. Luo, J. Wu, T. Zhou, J. Mao, L. Zhang, C. Zhang, Z. Guo, *Adv. Funct. Mater.* 2024, **34**, 2214538.

14 H. Tian, J.-L. Yang, Y. Deng, W. Tang, R. Liu, C. Xu, P. Han, H. J. Fan, *Adv. Energy Mater.* 2023, **13**, 2202603.

15 T. Zhou, Y. Mu, L. Chen, D. Li, W. Liu, C. Yang, S. Zhang, Q. Wang, P. Jiang, G. Ge, H. Zhou, *Energy Storage Mater.* 2022, **45**, 777.

16 J. Xu, W. Lv, W. Yang, Y. Jin, Q. Jin, B. Sun, Z. Zhang, T. Wang, L. Zheng, X. Shi, B. Sun, G. Wang, *ACS Nano* 2022, **16**, 11392.

17 J. Chen, G. Ou, P. Liu, W. Fan, B. Li, Z. Hu, Z. Wen, Y. Zhang, Y. Tang, X. Liu, M. Ye, C. C. Li, *Angew. Chem. Int. Ed.* 2025, **64**, e202414166.

18 T. Li, S. Hu, C. Wang, D. Wang, M. Xu, C. Chang, X. Xu, C. Han, *Angew. Chem. Int. Ed.* 2023, **62**, e202314883.

19 R. Zhao, H. Wang, H. Du, Y. Yang, Z. Gao, L. Qie, Y. Huang, *Nat. Commun.* 2022, **13**, 3252.

20 Q. Zong, R. Li, J. Wang, Q. Zhang, A. Pan, *Angew. Chem. Int. Ed.* 2024, **63**, e202409957.

21 H. Ni, Z. Fan, J. Wang, Y. Wu, *Energy Storage Mater.* 2025, **77**, 104220.

22 X. Pu, B. Jiang, X. Wang, W. Liu, L. Dong, F. Kang, C. Xu, *Nano-Micro Lett.* 2020, **12**, 152.

23 Y. Wang, N. Li, H. Liu, H. Sun, Z. Wang, L. Zhai, K. Chen, L. Mi, Z. Fang, Y. Huang, *J. Mater. Chem. A* 2024, **12**, 7799.

24 H. Liu, Z. Li, B. Sui, Q. Bao, P. Wang, Z. Gong, Y. Zhang, Y. Wu, F. Shi, M. Zhou, K. Zhu, *Industrial & Engineering Chemistry Research* 2024, **63**, 13611.

25 Z. Shen, Y. Liu, Z. Li, Z. Tang, J. Pu, L. Luo, Y. Ji, J. Xie, Z. Shu, Y. Yao, N. Zhang, G. Hong, *Adv. Funct. Mater.* 2025, **35**, 2406620.

26 Y. Yang, Z. Wei, S. Hu, B. Tang, G. Qu, C. Yue, X. Li, C. Han, *Adv. Energy Mater.* 2025, **15**, 2404367.